5-13-2006

Damage and Stress State Influence on Bauschinger Effect in Aluminum Alloys

J Brian Jordon

DAMAGE AND STRESS STATE INFLUENCE ON BAUSCHINGER EFFECT IN ALUMINUM ALLOYS

By

J. Brian Jordon

A Thesis
Submitted to the Faculty of
Mississippi State University
in Partial Fulfillment of the Requirements
for the Degree of Master of Science
in Mechanical Engineering
in the Department of Mechanical Engineering

Mississippi State, Mississippi

May 2006

DAMAGE AND STRESS STATE INFLUENCE ON BAUSCHINGER

EFFECT IN ALUMINUM ALLOYS

By

J. Brian Jordon

Approved:

Mark F. Horstemeyer Center for Advanced Vehicular Systems Chair in Computational Solid Mechanics Professor of Mechanical Engineering (Major Professor)	James C. Newman, Jr. Professor of Aerospace Engineering (Committee Member)
Steven R. Daniewicz Professor of Mechanical Engineering (Committee Member)	John M. Papazian Northrop Grumman (Committee Member)
Steven R. Daniewicz Graduate Coordinator of the Department Engineering	Kirk H. Schulz Dean of the College of Engineering

Name: J. Brian Jordon

Date of Degree: May 6, 2006

Institution: Mississippi State University

Major Field: Mechanical Engineering

Major Professor: Dr. Mark F. Horstemeyer

Title of Study: DAMAGE AND STRESS STATE INFLUENCE ON BAUSCHINGER EFFECT IN ALUMINUM ALLOYS

Pages in study: 51
Candidate for degree of Master of Science

In this work, the Bauschinger effect is shown to be intimately tied not only to plasticity but to damage as well. The plasticity-damage effect on the Bauschinger effect is demonstrated by employing different definitions (Bauschinger Stress Parameter, Bauschinger Effect Parameter, the Ratio of Forward-to-Reverse Yield, and the Ratio of Kinematic-to-Isotropic Hardening) for two differently processed aluminum alloys (rolled and cast) in which specimens were tested to different prestrain levels under tension and compression. Damage progression from second phase particles and inclusions that were generally equiaxed for the cast A356-T6 aluminum alloy and elongated for the rolled 7075 aluminum alloy was quantified from interrupted experiments. Observations showed that the Bauschinger effect had larger values for compression prestrains when compared to tension. The Bauschinger effect was also found to be a function of damage to particles/inclusions, dislocation/particle interaction, the work hardening rate, and the Bauschinger effect definition.

DEDICATION

I would like to dedicate this work to my son, Andrew, who was born during my second year of graduate school.

ACKNOWLEDGMENTS

I would like to thank the people who helped make this Master's Thesis possible. First, I would like to thank my advisor Dr. Mark Horstemeyer, who without his advice and input, this thesis would not be possible. I would also like to thank Dr. Steven Daniewicz, and Dr. James Newman, Jr., and Dr. John Papazian for their advice in the writing of this thesis. I would like to thank Northrop Grumman for allowing me to use their lab to conduct my research and Bob Fidnarick for introducing me to the experimental side of research. I would like to extend special thanks to Dr. Gabriel Potirniche, Dr. Yibin Xue, Dr. Yossef Hammi, and Kiran Solanki for their help with finite element simulations. Additionally, I would like to thank my wife, Amy, for all of the support she gave during the late nights and long weekends. Finally, I want to thank the Lord for His unfailing goodness and grace on my life.

TABLE OF CONTENTS

Page

DEDICATION i

ACKNOWLEDGMENTS ii

TABLE OF CONTENTS iii

LIST OF TABLES v

LIST OF FIGURES vi

CHAPTER

I. INTRODUCTION 1

Bauschinger Effect Parameters 5

II. MATERIAL MODEL 7

Introduction 7
Plasticity Model Formulation 8
Damage Model Formulation 11
Numerical Implementation 15
Ratio of Kinematic to Isotropic Hardening 19

III. MATERIALS AND EXPERIMENTS 21

Materials 21
Specimen Design and Experimental Setup 23

IV. EXPERIMENTAL RESULTS 26

Bauschinger Effect Stress-Strain Results 26
Bauschinger Effect Parameter Observation 29

V. MATERIAL MODEL ANALYSIS 35

Model Correlation 35
Void Nucleation Correlation 37

VI. DISCUSSION 40

VII. SUMMARY AND CONCLUSIONS 44

VIII. REFERENCES 46

APPENDIX

A A356-T6 and 7075-T651 Model Constants 49

LIST OF TABLES

TABLE Page

3.1. Chemical Composition and Elongation at Failure for 7075-T651 and A356-T6 Aluminum Alloys 24

4.1. Comparing BSP, and ratio of kinematic to isotropic hardening for the Bauschinger tests at various pre-strain levels for 7075-T651 and A356-T6 aluminum alloys. 34

A.1. Microstructure-property (elastic-plastic) model constants for A356-T6 and Aluminum 7075-T651 50

A.2. Microstructure-property (damage) model constants for A356-T6 and 7075-T651 aluminum alloys. 51

LIST OF FIGURES

FIGURE Page

1.1 A stress-strain curve that exhibits the Bauschinger effect for typical metallic alloys (Xiang and Vlassak, 2005). 3

2.1 Schematic of the fictitious material with increasing nucleation density and void growth of a model framework (Horstemeyer, 1999) 12

3.1 Optical micrograph of the grain structure in the rolling direction of 7075-T651 aluminum alloy..... 21

3.2 Optical micrograph A356-T6 cast aluminum alloy which shows second phase particles (Horstemeyer *et al*., 2003)..... 23

3.3 High cycle fatigue specimen design employed for the Bauschinger Effect experiments on the 7075-T651 alloy..... 24

4.1 Half-cycle true-stress true-strain data for 7075-T651 longitudinal direction comparing the compression followed by tension to tension followed by compression. 27

4.2 Half-cycle true-stress true-strain data for A356-T651 comparing the compression followed by tension to tension followed by compression. 28

4.4 The Bauschinger Effect Definition (BED) plotted versus the maximum forward pre-strain reached before reversal. 31

4.5 The Bauschinger Stress Parameter (BSP) and Ratio of Kinematic and Isotropic Hardening (RKI) plotted versus the maximum forward pre-strain reached before reversal for 7075-T651 and A356-T6. 32

4.6 A plot of the Bauschinger Stress Parameter (BSP) as a function of the maximum forward pre-strain reached before reversal. 33

FIGURE Page

5.1 The one-element FE model using an ISV plasticity-damage model is able to capture the Bauschinger effect for 7075-T651 wrought aluminum alloy 36

5.2 The one-element FE model using an ISV plasticity -damage model is able to capture the Bauschinger effect for A356-T6 cast aluminum alloy..... 37

5.3 A comparison of the damage nucleation model and experimental data of the void/crack density versus strain for A356-T6 and 7075-T651. The plot shows greater void/crack nucleation for tension than compression for cast A356 aluminum alloy 38

6.1. The experimental and finite element model of the Ratio of Kinematic and Isotropic Hardening (RKI) plotted versus the maximum forward prestrain reached before reversal for 7075-T651 and A356-T6. 42

CHAPTER I

INTRODUCTION

For metals that experience plastic deformation, the mechanical response depends on its deformation history not just on its current stress state (cf. Woolley, 1953; Able and Muir, 1972; Stoltz and Pelleoux, 1976; Lloyd, 1977; Pedersen *et al*., 1981; Rao and Murty, 1982; Embury, 1985; Corbin *et al*., 1996; Caceres *et al*., 1996; Reynolds and Lyons, 1996; Horstemeyer, 1998; Miller *et al*., 1999). This history can manifest changes in the mechanical response, like a difference between the yield stress in tension and compression as illustrated in Fig. 1.1, a schematic stress-strain curve for a ductile material. The stresses σ_f and σ_r are the forward and reversed flow stresses, respectively. If both the forward and reverse flow stresses are equal, the material behaves in an isotropic manner. However, experiments have shown that in many ductile materials, the flow stress in the reverse direction has more permanent softening than the flow stress of forward direction. This reduced reverse flow is known as the Bauschinger effect (Bauschinger, 1881).

The definition of the yield point can affect the Bauschinger effect. Specifically, a yield criterion based on the deviation from proportionality or a very small strain offset will imply a large Bauschinger effect while one that is based on a relatively large strain

offset or on a backward extrapolated yield stress can lead to a barely noticeable Bauschinger effect (Shiratori *et al*., 1979).

The Bauschinger effect has been found to be a function of several parameters (loading path, strain rate, temperature and texture) (Ono *et al*., 1983; Arsenault and Wu, 1987; Thakur and Nemat-Nasser, 1996;)**.** The physical sources attributed to the Bauschinger effect during the reverse loading of a material can be generalized into long-range and short-range transients. The long-range transients include dislocation interactions (Pedersen *et al*., 1981; Hasegawa *et al*., 1986) dislocation pile-ups at grain boundaries (Ono *et al*., 1983; Margolin *et al*., 1983), and Orowan loops around strong precipitates (Brown and Stobbs, 1971a; Brown and Stobbs, 1971b; Atkinson *et al*., 1974; Brown, 1977; Aran *et al*., 1987). The short-range transients include dislocation resistance to motion or annihilation (Aran *et al*., 1987). The Bauschinger effect can also be attributed to the influence of microstructural features such as void volume fraction and the size and shape of second phase particles (Embury, 1985; Reynolds *et al*., 1996).

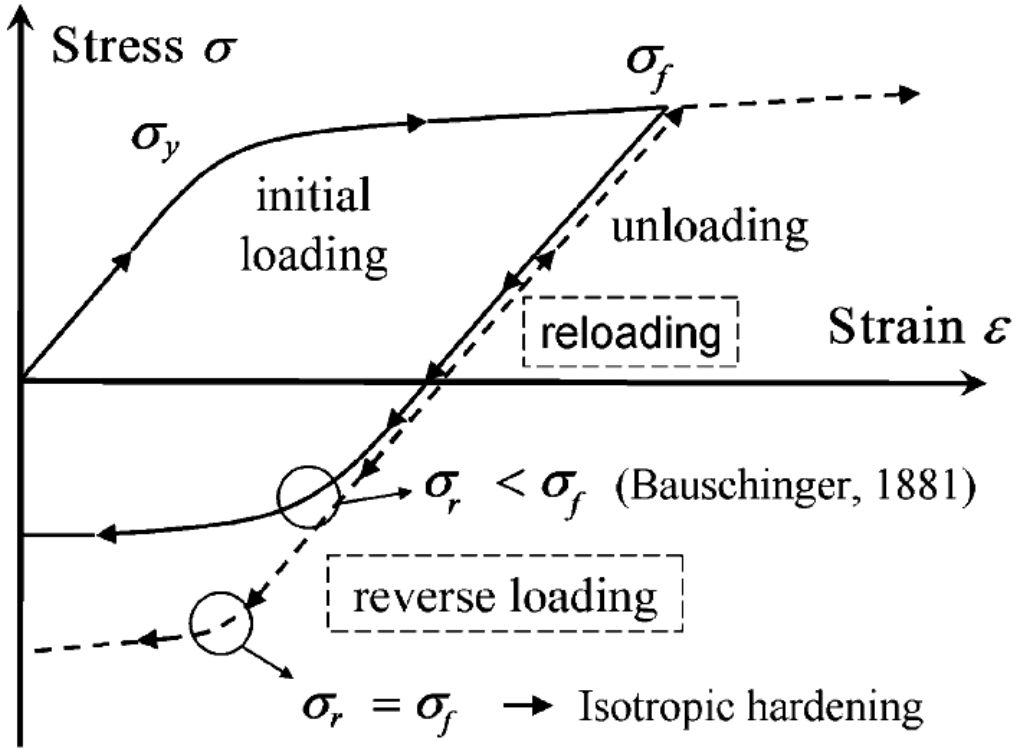

Figure 1.1. A stress-strain curve that exhibits the Bauschinger effect for typical metallic alloys (Xiang and Vlassak, 2005).

Many experimental and theoretical efforts have been devoted to studying the Bauschinger effect in bulk metals since the phenomenon was first reported (Masing *et al*., 1923; Brown and Stobbs, 1971a; Brown and Stobbs, 1971b; Atkinson *et al*., 1974; Stoltz and Pelloux, 1976; Brown, 1977; Margolin *et al*., 1978; Sowerby *et al*., 1979; Hasegawa *et al*., 1986; Bate and Wilson, 1986; Aran *et al*., 1987). More specifically, the reverse yield effect has been observed on many types of aluminum alloys, including reinforced ones (cf. Stoltz and Pelleoux, 1976; Lloyd, 1977; Embury, 1985; Caceres *et al*., 1996; Corbin *et al*., 1996; Reynolds and Lyons, 1996; Horstemeyer, 1998). Stoltz and Pelloux (1976) showed that alloys with nonshearable precipitates have a greater Bauschinger

effect then for the same alloy with shearable precipitates. Arsenault and Wu (1987) studied the contribution of SiC wiskers in a wrought 6061 aluminum alloy. Their work showed that as the volume fraction of SiC increased, the magnitude of Bauschinger effect also increased.

In addition to tension-followed-by-compression or compression-followed-by-tension tests, the Bauschinger effect has been observed in torsion-followed-by-tension experiments (Rao and Murty, 1982; Embury, 1985). The Bauschinger effect has also been observed at very high strain rates ($300s^{-1}$) by Thakur *et al*., (1996), who reported that metals that do not exhibit a Bauschinger effect in the quasi-static strain rate regime can exhibit a Bauschinger effect in very high strain rates regime.

Sleeswyk and Kemerink (1985) explained the Bauschinger effect in terms of dislocations motion between barriers. Upon strain reversal, statistically stored dislocations that were previously restricted move back over their free path. The other dislocations run into new barriers and induce an internal back stress. Stout and Rollett (1990) suggested that the observed Bauschinger effect in FCC metals can be attributed to isotropic hardening arising from dislocation substructure. They delineate the behavior into two categories: materials that deform by planar slip and those that deform by forming a “cell” and have a wavy slip pattern. The materials that fall into the planar slip category were dependent on the fact that the dislocation barriers were shearable or rigid.

Bauschinger Effect Parameters

Over the years, many different definitions have been used to quantify the magnitude of Bauschinger effect. Abel (1987) introduced two parameters as a function of the prestrain called the Bauschinger Stress Parameter (BSP) and Bauschinger Energy Parameter (BEP). Caceres *et al*. (1996) explains that the BSP is a parameter that quantifies the amount of back stress that particles exert on dislocations within the matrix. In aluminum, dispersed particles effect the work hardening rate because the back stress during reversal increases linearly due to the unrelaxed plastic strain around these particles. In addition, the work hardening is affected by non-linear hardening associated with the plastic relaxation of the matrix (Moan and Embury, 1979; Sowerby and Uko, 1979; Embury, 1987; Caceres *et al*., 1996). The BSP is defined as

$$BSP = \frac{|\sigma_f| - |\sigma_r|}{|\sigma_f|} \tag{1-1}$$

where σ_f is the forward pre-strain stress, and σ_r is the reversal stress**.**

The BEP is useful in illustrating the relationship between the kinematic and isotropic hardening that is observed during deformation. Moreover, the BEP can provide insight into how much anisotropy takes place in the material during a reverse yield test (Horstemeyer, 2001). The BEP is defined as

$$BEP = \tfrac{1}{2}\left\{\frac{|\sigma_f| - |\sigma_r|}{|\sigma_f| - |\sigma_y|}\right\} \tag{1-2}$$

where σ_y is the forward yield stress.

In slightly modifying Bauschinger's equation of the difference between forward yield and reverse yield, the difference is normalize by the forward yield stress and called the Bauschinger Effect Definition (BED),

$$BED = \frac{\sigma_y - \sigma_r}{\sigma_y} \tag{1-3}$$

In this study the damage state on the Bauschinger effect is illustrated and an internal state variable plasticity damage model is employ to capture the behavior for the rolled 7075-T651 aluminum alloy and cast A356 aluminum alloy. Literature to date has focused on plasticity related to dislocation motion. Several authors have employed internal state variables to model the Bauschinger in ductile metals (Mollica *et al*., 2001; Chateau *et al*., 2005). Both Mollica *et al*. (2001) and Chateau *et al*. (2005) employed a form of kinematic and isotropic state variables, however, neither included a damage state that was influenced by cracked or debonded second phase particles or inclusions. To the best of the author's knowledge, there exists no model that captures the Bauschinger effect in terms of plasticity as a function of dislocation motion and damage accumulation.

CHAPTER II

MATERIAL MODEL

Introduction

The internal state variable (ISV) plasticity-damage model presented by Bammann and Aifantis (1989) and Bammann *et al*. (1996) and later modified to account for nucleation, growth, and coalescence by Horstemeyer and Gohkale (1999) and Horstemeyer *et al*., (2000) has been used to predict the plastic deformation of many types of metals under various loading conditions (cf. Horstemeyer, 2001). This plasticity-damage model has been implemented into several finite element codes and applied to various industrial applications (cf. Horstemeyer and Wang, 2003). The ISV model is a physically based plasticity and damage constitutive model that includes microstructural content and is consistent with continuum level kinematics, kinetics, and thermodynamics. As a result, the ISV model can capture the Bauschinger effect because of the plasticity (kinematic and isotropic hardening) and damage (arising from cracked or debonded particles) (Horstemeyer, 2003).

Miller *et* al. (1999) employed the ISV model for small-to-moderate strains for a 304L SS alloy in which they did not use damage, although they modified the hardening equations. However, they did not study compression-followed-by-tension, they only studied tension-followed-by-compression.

Plasticity Model Formulation

The ISV model employs kinematics that assumes a multiplicative decomposition of the deformation gradient into the deviatoric plastic, dilational plastic, and elastic parts. The symmetric and skew symmetric parts of velocity gradient are decomposed into elastic and plastic parts. The rate of deformation is the symmetric tensor and is defined as

$$\underline{D} = \underline{D}^e + \underline{D}^p + \underline{D}^v, \tag{2-1}$$

where the $\underline{D}^e$ is the elastic part, $\underline{D}^p$ is the deviatoric plastic, and $\underline{D}^v$ is the volumetric part. The spin tensor is the skew symmetric tensor and is defined as

$$W = \underline{W}^e + \underline{W}^p, \tag{2-2}$$

where $\underline{W}^e$ is the plastic part and $\underline{W}^p$ is the deviatoric plastic part. It is important to note that the volumetric spin, $\underline{W}^v$, is assumed to be zero. It is important to note that any second order tensor variable $\underline{X}$, $\dot{\underline{X}}$ represents an objective rate, and for any scalar variable X, $\dot{X}$ represents a time rate of change.

Linear elasticity, with respect to the natural configuration, is defined as

$$\overset{\circ}{\underline{\sigma}} = \dot{\underline{\sigma}} - \underline{W}^e \underline{\sigma} - \underline{\sigma}\underline{W}^e = \lambda(1-D)tr(\underline{D}^e)\underline{I} + 2\mu(1-D)\underline{D}^e - \frac{\dot{D}}{1-D}\underline{\sigma} \tag{2-3}$$

where the Cauchy stress is σ, the elastic spin is W^e, and λ and μ are the elastic Lame constants. The elastic rate of deformation is given by $\underline{D}^e$, and $\underline{D}$ represents the total deformation. The yield function is used to determine whether the state of stress is elastic or plastic. If the state of stress is plastic, the deviatoric inelastic flow rule is employed.

The deviatoric inelastic flow rule (Equation 2-4) captures the effect of creep and plasticity in terms of kinematic and isotropic hardening, temperature, and damage as a function of void volume.

$$\underline{D}_d^p = f(T)\sinh\left[\frac{\left\|\underline{\sigma}' - \underline{\alpha}\right\| - \{R + Y(T)\}\{1-D\}}{V(T)\{1-D\}}\right]\frac{\underline{\sigma}' - \underline{\alpha}}{\left\|\underline{\sigma}' - \underline{\alpha}\right\|} \tag{2-4}$$

The function $f(T)$ affects the point at which the rate affects yield. The function $Y(T)$ is the yield stress independent of rate. The function $V(T)$ determines the magnitude of the rate-dependence on yielding. These functions are determined from simple monotonic experimentation at different strain rates and temperatures.

$$Y(T) = C_1 \exp\left(-C_2/T\right), \tag{2-5}$$

$$f(T) = C_3 \exp\left(-C_4/T\right), \tag{2-6}$$

$$V(T) = C_5 \exp\left(-C_6/T\right), \tag{2-7}$$

where C_1 through C_6 are model constants.

In terms of plasticity, the kinematic hardening internal state variable (α) and the isotropic hardening internal state variable (R) are given in Equations (2-8) and (2-9), respectively. In this model, the kinematic hardening and recovery describe the effects of local dislocation interaction with barriers such as grain boundaries and second phase particles. This anisotropic hardening is seen as a shift of the yield surface center. The effects of statistically stored dislocations on the global scale is captured in the isotropic

hardening and results in an uniform growth of the yield surface. Both kinematic and isotropic hardening equations are in a hardening minus recovery format and are given by,

$$\underline{\dot{\alpha}} = \left\{ h(T)\underline{D}^p - \left[\sqrt{\frac{2}{3}} r_d(T) \left\| \underline{D}^p \right\| + r_s(T) \right] \|\underline{\alpha}\| \underline{\alpha} \right\} \left(\frac{GS_0}{GS} \right)^Z, \tag{2-8}$$

$$\dot{R} = \left\{ H(T) \left\| \underline{D}^p \right\| - \left[R_d(T) \left\| \underline{D}^p \right\| + R_s(T) \right] R^2 \right\} \left(\frac{GS_0}{GS} \right)^Z. \tag{2-9}$$

The $h(T)$ and $H(T)$ are scalar functions that are the anisotropic and isotropic hardening moduli, respectively. The scalar functions $r_s(T)$ and $R_s(T)$ represent diffusion-controlled static or thermal recovery. The $r_d(T)$ and $R_d(T)$ functions describe dynamic recovery relating to the annihilation of dislocations that take place in plastic deformation, and are scalar in nature. The microstructure effect of grain size on the plastic flow behavior is captured by the *GS* parameter. The isotropic and anisotropic hardening and recovery functions are given by,

$$r_d(T) = C_7 \left(1 + C_{19} \left[\frac{4}{27} - \frac{J_3'^2}{J_2'^3} \right] \right) \exp\left(-C_8 / T \right), \tag{2-10}$$

$$h(T) = \left\{ C_9 \left(1 + C_{20} \left[\frac{4}{27} - \frac{J_3'^2}{J_2'^3} \right] \right) \right\} - C_{10} T, \tag{2-11}$$

$$r_s(T) = C_{11} \exp\left(-C_{12} / T \right), \tag{2-12}$$

$$R_d(T) = C_{13} \left(1 + C_{21} \left[\frac{4}{27} - \frac{J_3'^2}{J_2'^3} \right] \right) \exp\left(-C_{14} / T \right), \tag{2-13}$$

$$H(T) = \left\{ C_{15} \left(1 + C_{22} \left[\frac{4}{27} - \frac{J_3^{'2}}{J_2^{'3}} \right] \right) \right\} - C_{16} T, \tag{2-14}$$

$$r_s(T) = C_{17} \exp\left(-C_{18} \big/ T \right), \tag{2-15}$$

where C_7 to C_{22} are model constants, $J_2^{'} = \frac{1}{2}\left(\underline{\sigma}^{'} - \underline{\alpha}\right)^2$ and $J_3^{'} = \frac{1}{3}\left(\underline{\sigma}^{'} - \underline{\alpha}\right)^3$. The deviatoric stress $\underline{\sigma}^{'}$ is expressed in indicial notation as $\sigma_{ij}^{'} = \sigma_{ij} - \frac{1}{3}\sigma_{ii}$.

Damage Model Formulation

The damage model is based on a void nucleation, growth and coalescence formulation, where the damage state is defined in terms of the change in the ratio of the volume of an element in the elastically unloaded state from the initial reference state. The damage parameter, in the intermediate configuration, can be written as

$$\phi = \frac{V_v}{V_2} = \frac{V_v}{N}\frac{N}{V_2} = v_v \eta, \tag{2-16}$$

where $V_v = \eta^* V_o v_v$, $V_2 = V_o - V_v$, $\eta = \eta^* \frac{V_o}{V_2}$, and $\eta^* = N / V_o$. In the above equations, V_o is the continuum material volume, v_v is the average void volume and N represents the total number of initial voids present. The damage framework employed by the model is best described by Fig 2.1. The model assumes that voids can nucleate by decohesion of the material matrix and/or particle fracture /debonding. The damage model also allows for initial voids to grow as expected in cast alloys under an applied stress state. In addition, the model allows void growth to occur at different sides of the cracked or

debonded particle, with the size of the newly initiated void assumed to be equal to the size of a second phase particle. Finally, void coalescence is added to the model to capture the process of multiple voids growing together, joining, and eventually resulting in ductile failure.

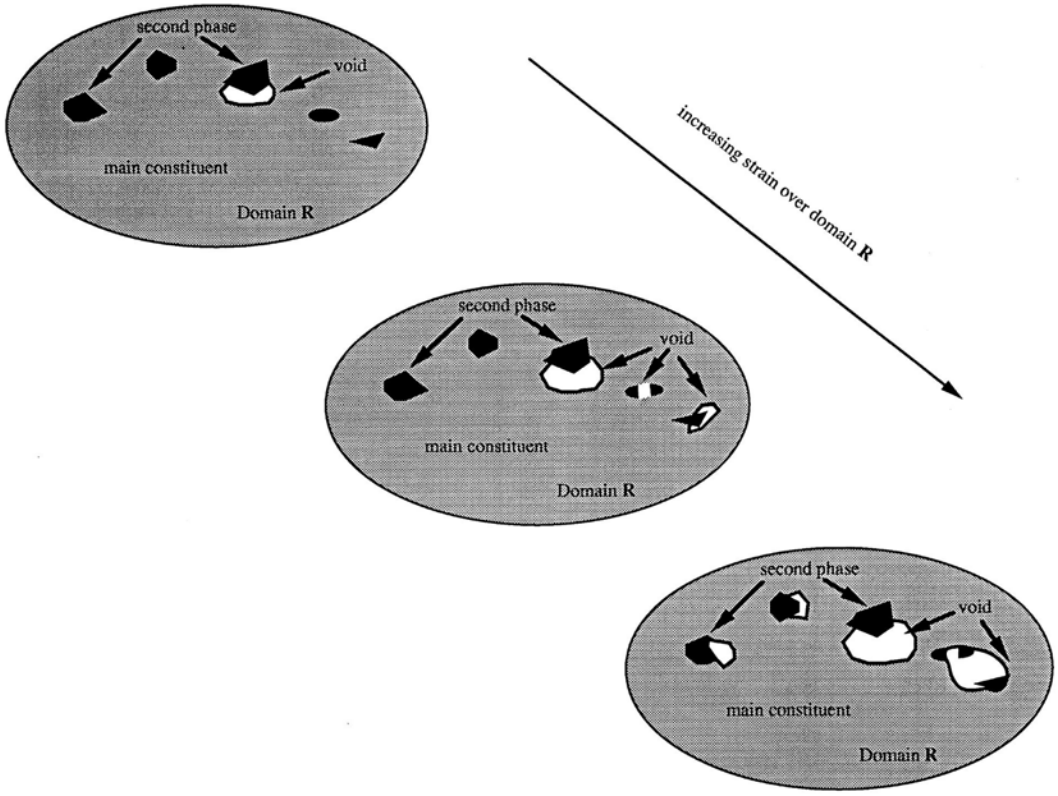

Figure 2.1. Schematic of the fictitious material with increasing nucleation density and void growth of a model framework (Horstemeyer, 1999)

The void nucleation rule follows the work done by Horstemeyer and Gohkale (1999) and is employed to capture the effect of voids nucleating under tension, compression, and torsion. The void nucleation function in the integrated form is given by,

$$\eta(t) = C_{coeff} \exp\left(\frac{\varepsilon(t) d^{1/2}}{K_{IC} f^{1/3}} \left\{ a\left[\frac{4}{27} - \frac{J_3^2}{J_2^3} \right] + b\frac{J_3}{J_2^{3/2}} + c\left\| \frac{I_1}{\sqrt{J_2}} \right\| \right\} \right) \exp\left(C_{\eta T} / T \right), \tag{2-17}$$

where C_{coeff} is a material constant, T is temperature, $\varepsilon(t)$ is the strain rate, and $C_{\eta T}$ is a temperature dependent material constant. The model constants a, b, and c are used to capture the effect of void fraction resulting from local internal stresses, and are determined from uniaxial tension, compression, and torsion experiments. The volume fraction of the second phase particles is captured by the f constant, d is the average size of the second phase particle, and K_{IC} is the fracture toughness. In order to effectively model the stress dependence on damage and distinguish between tension, compression and torsion void nucleation rates, deviatoric stress invariants were employed (Horstemeyer and Gokhale, 1999): $I_1 = \sigma_{kk}$; $J_2 = \frac{1}{2} S_{ij} S_{ij}$; $J_3 = S_{ik} S_{ij} S_{ki}$; where $S_{ij} = \sigma_{ij} - \frac{1}{3}\delta_{ij}\sigma_{kk}$.

The void growth rule (Equation 2-18) used in this model is the void volume fraction rate developed by Cocks and Ashby (1981), where m is a void growth constant, σ_H is the hydrostatic stress, σ_{vm} is the von Mises stress, and ϕ_{pore} is related to the casting porosity. The Cocks and Ashby equation is employed to model the growth of large voids and is largely dependent on stress triaxiality (Equation 2-19).

$$\phi_{pores} = 1 - \left[1 + \left[\left(1 - \phi_{pores}\right)^{1+\frac{V(T)}{Y(T)}} - 1 \right] \exp \beta\chi\varepsilon(t) \left(1 + \frac{V(T)}{Y(T)} \right) \right]^{\frac{1}{1+\frac{V(T)}{Y(T)}}}, \tag{2-18}$$

$$\chi = \frac{\sigma_H}{\sigma_{vm}} \tag{2-19}$$

A separate void growth rule is applied the growth of newly nucleated voids from cracked and/or debonded particles. The integrated formulation is taken from McClintock (1968) and is shown as

$$v = \frac{4}{3}\pi\left[\varepsilon(t)\sqrt{\frac{3}{2(1-n)}}\sinh\left(\sqrt{3}(1-n)\frac{\sqrt{2}I_1}{3\sqrt{J_2}}\right)\right]^3, \tag{2-20}$$

where n is strain hardening constant and R_0 is the initial radius of the voids.

The coalescence of two voids growing together and becoming one has a compound relationship between the nucleation and growth terms (Equation 2-21). The C_{CT} parameter is a material constant, C_{D1} relates to the simple case where two voids grow together and become one and C_{D2} relates the second case where smaller voids nucleating and growing are influenced by nearby larger voids nucleating and growing.

$$C = \left[C_{D1} + C_{D2}\eta v\right]\left(GS_0/GS\right)^Z\left(C_{CT}T\right), \tag{2-21}$$

Finally total damage incorporates the nucleation, void growth and coalescence terms and is presented in Equation 2-22:

$$\phi = \left(\eta v + \phi_{pore}\right)C \tag{2-22}$$

The rate formulation of the damage equations in terms of the observable and state variables and are given in Equation 2-23 through 28:

$$\dot{D} = \left[\dot{\phi}_{particles} + \dot{\phi}_{pores}\right]C + \left[\phi_{particles} + \phi_{pores}\right]\dot{C} \tag{2-23}$$

$$\dot{\phi}_{particles} = \dot{\eta}v + \eta\dot{v} \tag{2-24}$$

$$\dot{\eta} = \left\| \underline{D}^P \right\| \frac{d^{1/2}}{K_{IC} f^{1/3}} \eta \left\{ a \left[\frac{4}{27} - \frac{J_3^2}{J_2^3} \right] + b \frac{J_3}{J_2^{3/2}} + c \left\| \frac{I_1}{\sqrt{J_2}} \right\| \right\} \exp\left(C_{\eta T} / T \right) \tag{2-25}$$

$$\dot{v} = \frac{\sqrt{3} R_0}{2(1-n)} \left[\sinh\left(\sqrt{3}(1-n) \frac{\sqrt{2} I_1}{3\sqrt{J_2}} \right) \right] \left\| D^P \right\| \tag{2-26}$$

$$\dot{\phi}_{pores} = \left[\frac{1}{(1-\phi_{pores})^m} - (1-\phi_{pores}) \right] \sinh\left\{ \frac{2\left(2^{V(T)/Y(T)} - 1 \right)}{\left(2^{V(T)/Y(T)} + 1 \right)} \frac{\sigma_H}{\sigma_{vm}} \right\} \left\| \underline{D}^P \right\| \tag{2-27}$$

$$\dot{c} = C_{coal} \left[\eta \dot{v} + \dot{\eta} v \right] \exp(C_{CT} T) \left(GS_0 / GS \right)^Z \tag{2-28}$$

The damage progression (Equation 2-23) includes the coalescence rate term (Equation 2-28) to account for particle-to-pore and pore-to-pore interactions. The particle volume fraction rate is described in Equation 2-24, which encompasses particle nucleation (Equation 2-25) and void growth (Equation 2-26).

Numerical Implementation

The modified ISV plasticity-damage model has been implemented in finite element codes such as DYNA2D, DYNA3D, PRONTO2D, PRONTO2D, JAC3D, NIKE2D, and ABAQUS (Bammann *et* al., 1993). The numerical implementation is based upon a flow rule derived from a numerical consistency condition. A brief explanation of a few finite element terms is necessary. The solution of a finite element code is based on an operator split. An operator split is a term that implies that the equilibrium during each time step is enforced, which allows the stress gradient to be determined. This, of course, is based upon the assumption that the state of stress remains constant through the time step. At the end of each step, the stress is updated. Bammann

(1993) suggested that in order to implement the ISV model, one more operator split must be added to account for the temperature and damage state that is introduced during the integration. By maintaining a constant damage value through each step, the stress is computed. During the next time step, the damage is recalculated based on the latest stress, velocity gradient, and internal state variables.

Kreig (1977) presented several numerical methods for solving a linear-elastic perfectly plastic isotropic model with a von Mises yield surface and associate flow rule. He showed that the radial return method was the most efficient method with a tolerable amount of numerical error. This same radial return method is then applied to the modified plasticity-damage model to achieve the maximum computational efficiency and as such, evaluate the stress integrals. In order to solve for the plastic part of the strain, the radial return method is employed, which assumes all strains are elastic and thus forces the plastic deformation gradient, $\underline{D}^P = 0$.

The first step of the numerical implementation requires determining the trial stresses and internal state variables while assuming that the strain remains elastic (Bammann *et* al., 1993). Horstemeyer (2001) states that in order to solve the hardening rate equations, the deviatoric plastic rate of deformation must be replaced with the total deformation, as shown in Equations 2-29 and 2-30:

$$\dot{\underline{\alpha}} = h(T)\underline{D}_d^P - [r_d(T)\sqrt{2/3}\|\underline{D}\| + r_s(T)]\sqrt{2/3}\|\underline{\alpha}\|\underline{\alpha} \tag{2-29}$$

$$\dot{R} = \sqrt{2/3}H(T)\left\|D_d^P\right\| - [R_d(T)\sqrt{2/3}\|\underline{D}\| + R_s(T)]|R|R \tag{2-30}$$

Now, the radial return method is used to give trial values for the deviatoric stress and the internal hardening variables. The N subscript represents the value of the time step and N+1 represents the value of time step at N+1.

$$\underline{\sigma}_{N+1}^{trial} = \underline{\sigma}'_N + \int_{t_N}^{t_{N+1}} 2\mu(1-\phi)\underline{D}'\,dt - \int_{t_N}^{t_{N+1}} \frac{\dot{\phi}\underline{\sigma}'}{1+\phi}dt \approx \underline{\sigma}'_N(1-\frac{\phi\Delta t}{1+\phi}) + 2\mu(1-\phi)\underline{D}'\Delta t \tag{2-31}$$

$$\underline{\alpha}_{N+1}^{trial} = \underline{\alpha}_N + \int_{t_N}^{t_{N+1}} (r_d\sqrt{2/3}\|\underline{D}\| + r_s)\sqrt{2/3}\|\underline{\alpha}\|\underline{\alpha}dt \approx \{1-(r_d\sqrt{2/3}\|\underline{D}\| + r_s)\sqrt{2/3}\|\underline{\alpha}\|\underline{\alpha}\Delta t\}\underline{\alpha}_N \tag{2-32}$$

$$R_{N+1}^{trial} = R_N + \int_{t_N}^{t_{N+1}} (R_d\sqrt{2/3}\|\underline{D}\| + R_s)|R|R \approx \{1-(R_d\sqrt{2/3}\|\underline{D}\| + R_s)\sqrt{2/3}|R|R\Delta t\}R_N \tag{2-33}$$

Next, the flow rule is defined,

$$\underline{D}_d^p = \sqrt{2/3}f(T)\sinh\left(\frac{\sqrt{3/2}\|\xi\| - (R - Y(T)(1-\phi)}{V(T)(1-\phi)}\right)\frac{\xi}{\|\xi\|} \tag{2-34}$$

where

$$\underline{\xi} = \underline{\sigma}^{trial} - 2/3\,\underline{\alpha} \tag{2-35}$$

The flow rule given in Equation (2-36) is inverted by taking the norm of both sides:

$$\Phi = \sqrt{3/2}\|\xi\| - (1-\Phi)[R + Y + V\sinh^{-1}(\frac{\sqrt{2/3}\|\underline{D}\|}{f})] = 0 \tag{2-36}$$

Bammann (1993) goes on to explain that if $\Phi^{trial} \le 0$, the stresses at step N+1 are updated to the trial values because the step was elastic. However, if $\Phi^{trial} > 0$ then plastic deformation has taken place and a correction to the trial deviatoric stress and the internal hardening variables are then reverted back to the new yield surface:

$$\sigma'_{N+1} = \sigma^{trial}_{N+1} + \int_{t_N}^{t_{N+1}} 2\mu(1-\phi)D^P dt = \sigma^{trial}_{N+1} - \frac{2\mu(1-\phi)\gamma}{\|\xi\|}\xi \tag{2-37}$$

$$\underline{\alpha}_{N+1} = \underline{\alpha}^{trial}_{N+1} + \int_{t_N}^{t_{N+1}} h(T)D^P dt = \underline{\alpha}^{trial}_{N+1} + \frac{h\gamma}{\|\xi\|}\xi \tag{2-38}$$

$$R_{N+1} = R^{trial}_{N+1} + \sqrt{2/3}\int_{t_N}^{t_{N+1}} H(T)\|D^P\|dt = R^{trial}_{N+1} + \sqrt{2/3}H\gamma \tag{2-39}$$

The updated trial values are then substituted back into the flow rule. Solving for γ so that $\Phi = 0$, gives the following equation:

$$\gamma = \frac{\|\xi\| - \sqrt{2/3}(1-\varphi)(Y + R + V\sinh^{-1}(\frac{\|D\|}{f})}{2\mu(1-\varphi) + 2/3\,(h + H(1-\varphi))} \tag{2-40}$$

Next, the total effective strain is calculated and given by

$$\varepsilon_{N+1} = \varepsilon_N + \sqrt{2/3\gamma} \tag{2-41}$$

The damage equations are updated by using the J_2 and J_3 from the corrected σ'_{N+1} and are shown below:

$$\eta_{N+1} = C_{coeff}\exp\left(\frac{\varepsilon_{N+1}d^{1/2}}{K_{IC}f^{1/3}}\left\{a\left[\frac{4}{27} - \frac{J_3^2}{J_2^3}\right] + b\frac{J_3}{J_2^{3/2}} + c\left\|\frac{I_1}{\sqrt{J_2}}\right\|\right\}\right)\exp\left(C_{\eta T}/T\right) \tag{2-42}$$

$$\phi_{pores\,N+1} = 1 - \left[1 + \left[\left(1-\phi_{pores}\right)^{1+\frac{V(T)}{Y(T)}} - 1\right]\exp\beta\chi\varepsilon_{N+1}\left(1 + \frac{V(T)}{Y(T)}\right)\right]^{\frac{1}{1+\frac{V(T)}{Y(T)}}} \tag{2-43}$$

$$v_{N+1} = \frac{4}{3}\pi\left[\varepsilon_{N+1}\sqrt{\frac{3}{2(1-n)}}\sinh\left(\sqrt{3}(1-n)\frac{\sqrt{2}I_1}{3\sqrt{J_2}}\right)\right]^3 \tag{2-44}$$

$$C_{N+1} = \left[C_{D1} + C_{D2}\eta_{N+1}\nu_{N+1}\right]\left(GS_0 / GS\right)^{Z}\left(C_{CT}T\right) \tag{2-45}$$

$$\phi_{N+1} = \left(\eta_{N+1}\nu_{N+1} + \phi_{pore\,N+1}\right)C_{N+1} \tag{2-46}$$

Finally, the total stress is calculated for that time step

$$\sigma_{N+1} = \sigma'_{N+1} + p_{N+1} \tag{2-47}$$

and the pressure is given as

$$p_{N+1} = \frac{1}{3}tr(\sigma_n)(1-\varphi) + (1-\varphi)\Delta t K tr(D) \tag{2-48}$$

The process is then repeated for each time step until the full step increment is complete. Bammann (1993) explains that within the ISV model, the damage ϕ term has a maximum limit of 1.0 that represents total failure.

Ratio of Kinematic to Isotropic Hardening

In order to quantify the Bauschinger effect in the experimental results, a von Mises yield surface is employed by inverting the kinetic equation, Equation (2-4), and ignoring the temperature and strain rate effects. The amount of kinematic and isotropic hardening can be quantified from the experimental data by using the definition of the yield surface

$$\left|\sigma_f - \alpha\right| - R - \sigma_y = 0 \tag{2-49}$$

$$\left|\sigma_r - \alpha\right| - R - \sigma_y = 0 \tag{2-50}$$

where σ_f and σ_r are the forward stress and reverse yield respectively, α is the kinematic hardening, R is the isotropic hardening, and σ_y is initial yield. Finally, the kinematic and

isotropic hardening relationships can be determined by rearranging Equations (2-49) and (2-50) into the following forms,

$$\alpha = \frac{\sigma_f + \sigma_r}{2} \tag{2-51}$$

$$R = \frac{\sigma_f - \sigma_r}{2} - \sigma_y \tag{2-52}$$

A parameter not previously presented in literature but useful in quantifying the Bauschinger during reverse yield experiments is the ratio of kinematic hardening to isotropic hardening (RKI). RKI is defined by dividing Equation (2-51) by Equation (2-52) and given by the following

$$RKI = \frac{\sigma_f + \sigma_r}{\sigma_f - \sigma_r} - 2\sigma_y \tag{2-53}$$

CHAPTER III

MATERIALS AND EXPERIMENTS

Materials

The materials experimentally tested in this research were 7075-T651 aluminum alloy and A356-T6 aluminum alloy.

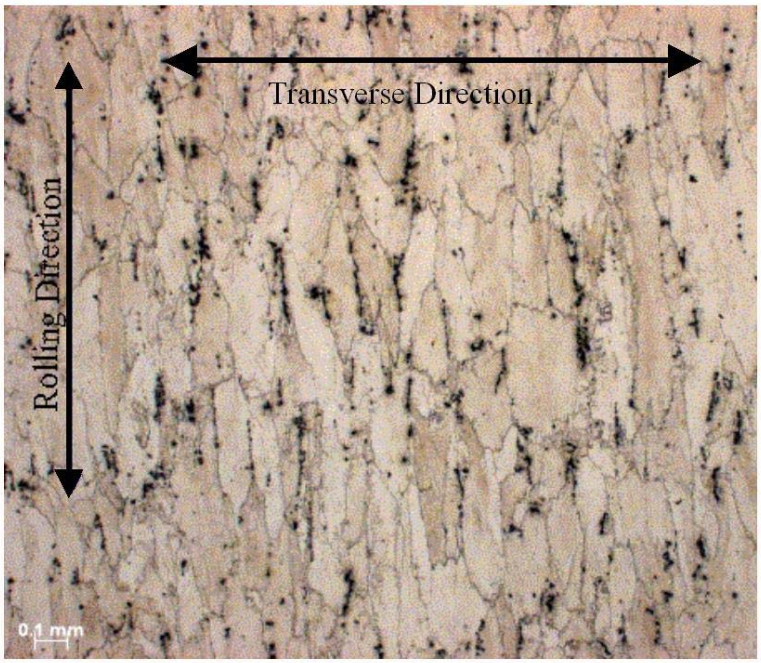

Figure 3.1. Optical micrograph of the grain structure in the rolling direction of 7075-T651 aluminum alloy.

The 7075-T651 is a fairly high strength aluminum alloy used heavily in the aircraft industry. The alloy was examined in its as-received condition using a scanning electron microscope and an optical microscope to quantify the particle size and grain size. The grains of this wrought material were found to be pancake shaped as displayed in Fig.

3.1. The pancake shaped grains were aligned in the rolling direction of the wrought plate and scattered throughout the alloy were Al_7Cu_2Fe and Fe_3SiAl_{12} constituent particles. The average size of these particles was approximately 2 microns, with a range of 1 to 25 microns. The aspect ratio for the particles was 4.5 with an average size of 18 by 4 microns and a void volume fraction of approximately of 2 percent. In addition, Mg_2Si constituent phases were also present with an approximate size of equal to or less than the Al_7Cu_2Fe particles. Also, many of these particles were broken during manufacturing process and distributed along the rolling direction creating a non-uniform distribution.

Similar to the wrought alloy, the cast A356-T6 was metallographically examined in the billet form using a scanning electron microscope and an optical microscope (Fig. 2b). Because no rolling procedure was applied to the material, the cast alloy was more isotropic compared to the wrought material as observed from the equiaxed particles and secondary dendrite arms. Second phase particles within the matrix ranged from 3 to 10 microns, and the silicon particles ranged form 4 to 70 microns. The aspect ratio for the particles was 1.0 with an average size of 4 microns and a void volume fraction of approximately of 7 percent.

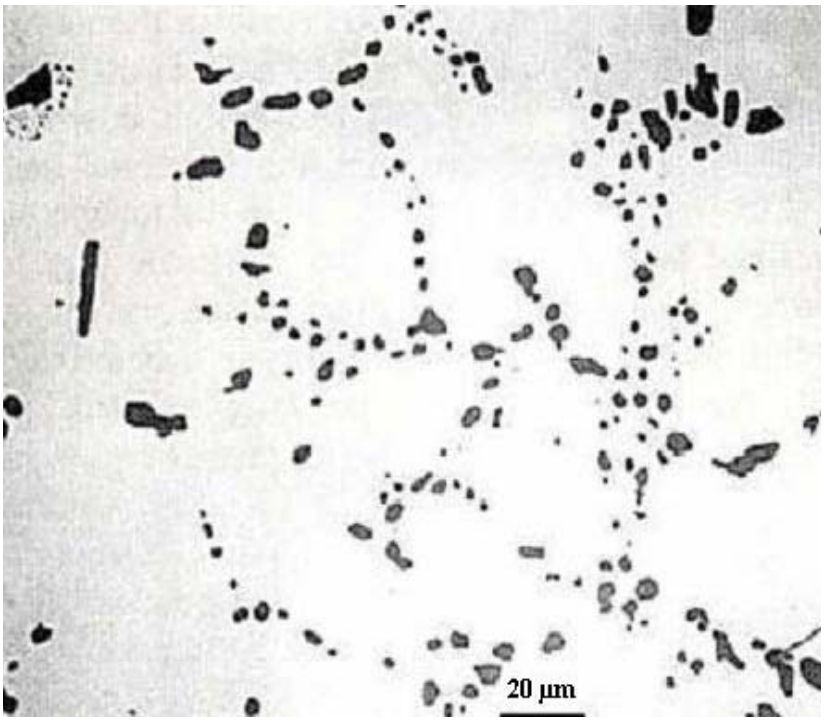

Figure 3.2. Optical micrograph A356-T6 cast aluminum alloy which shows second phase particles (Horstemeyer *et al*., 2003).

Specimen Design and Experimental Setup

Cylindrical low cycle fatigue type specimens with a uniform gage length were used for both alloys and were designed based on ASTM standard E606. For the A356-T6, the specimens were machined from the chilled end of the cast billet and had an outer diameter of 9.525 mm. Mechanical experiments were conducted with a strain rate of 0.0001/sec in an ambient laboratory environment. Specimens with an outer diameter of 10.135 mm (Fig. 3.3) were used to test the 7075-T651 and were machined from the longitudinal direction of the two-inch-thick plate. The strain rate was 0.001/sec and the temperature was ambient. Table 1 lists the chemical composition and tensile elongation at failure for the wrought 7075-T651 aluminum and the cast A356-T6 aluminum alloys.

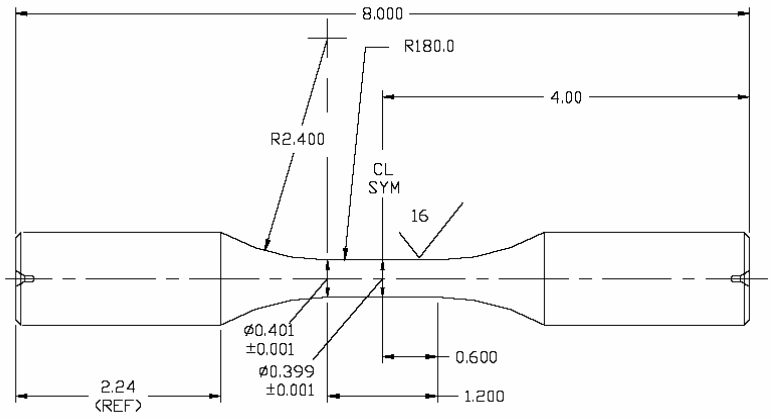

Figure 3.3. High cycle fatigue specimen design employed for the Bauschinger Effect experiments on the 7075-T651 alloy.

Table 3.1. Chemical Composition and Elongation at Failure for 7075-T651 and A356-T6 Aluminum Alloys

Aluminum Alloy	Chemical Composition	Tensile Elongation at Failure (%)
7075-T651	Al-5.6Zn-2.5Mg-1.6Cu	14.7
A356-T6	Al-7.5Si-0.5Fe-0.35Mg	8.2

The reverse tests were conducted using a 4 column, 50 kip MTS frame. The frame had cylindrical collet grips that ensured proper alignment of the specimen so as to not introduce bending. The axial alignment of each frame was checked by using an alignment specimen and measuring the deflection of the specimen under load. The frame was aligned to within 0.001 inch of deflection.

The load cell was set at a full-scale range of 25 kips. The load cell was calibrated to within 1% error reading through the full-scale range. A MTS fatigue rated knife blade axial extensometer was used for the strain measurement. The extensometers were set at a full scale of 10% maximum strain and calibrated to better than 1% of the

reading over the full range. The MTS controller application, called Multipurpose Test Ware (MPT), was used for programming the test, controlling the experiment, and for data collection. The data acquisition of the MTS system was set to record data in a linear form.

Two types of experiments to observe the Bauschinger effects were conducted. First the cylindrical specimens were prestrained in tension, then uniaxially reloaded in compression. The second kind included a different set of specimens that were prestrained in compression, then uniaxially reloaded in tension. For the wrought material, three strain levels were tested: 1%, 2.5%, 5%. For the cast material, three strain levels were tested: 2%, 3%, 5%.

In addition, interrupted experiments were performed to determine the void nucleation rate of the cast and wrought alloys. Tensile and compression specimens were loaded monotonically to pre-determined strain levels and sectioned for void and/or crack density quantification. The cracked and debonded particles were then quantified as a function of applied strain (Gall and Horstemeyer, 2000).

CHAPTER IV

EXPERIMENTAL RESULTS

Bauschinger Effect Stress-Strain Results

The results of the reverse yield experiments for the 7075-T651 and A356-T6 are shown in Figure 4.1 and Figure 4.2, respectively. Several visual differences between the flow stress for both alloys were observed. In tension-followed-by-compression the 7075-T651 had a sharp initial yield in tension, but the reverse yield in compression resulted in a larger flow stress knee. However, for the compression-followed-by-tension, the yield knee in tension was much larger than the TC sequence. In contrast, for A356-T6 alloy, the yield knees for compression and tension were both large and did not vary by sequence. Fig. 4.3 illustrates the difference between the flow stress of tension and compression for both alloys.

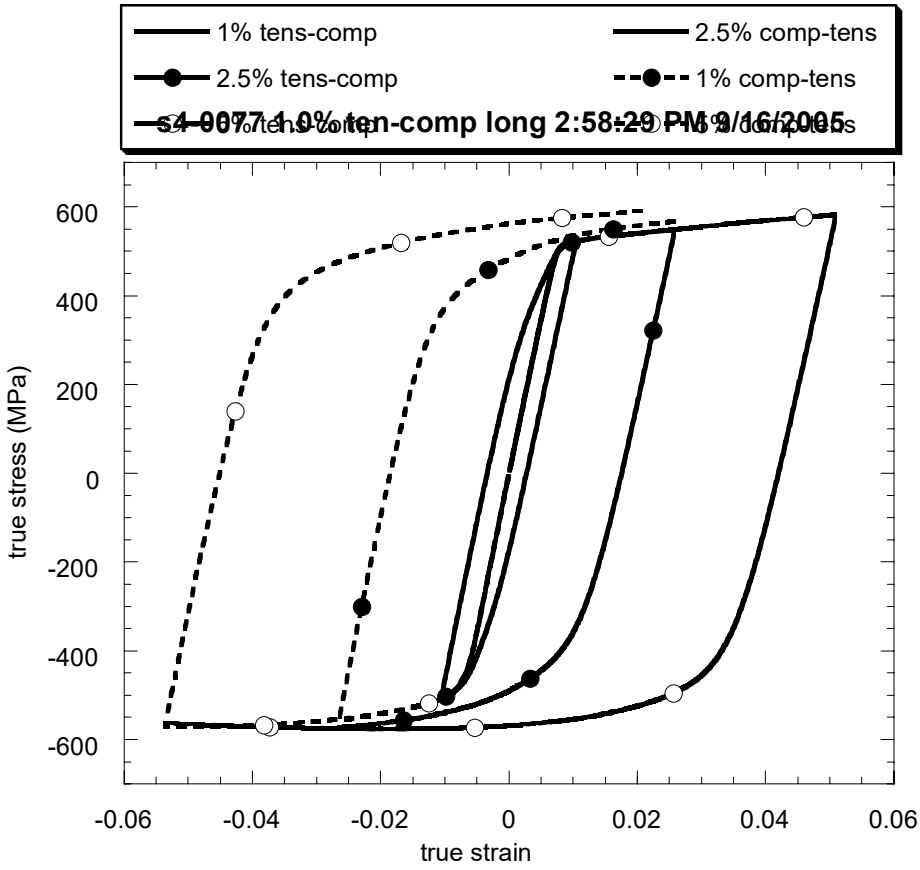

Figure 4.1. Half-cycle true-stress true-strain data for 7075-T651 longitudinal direction comparing the compression followed by tension to tension followed by compression.

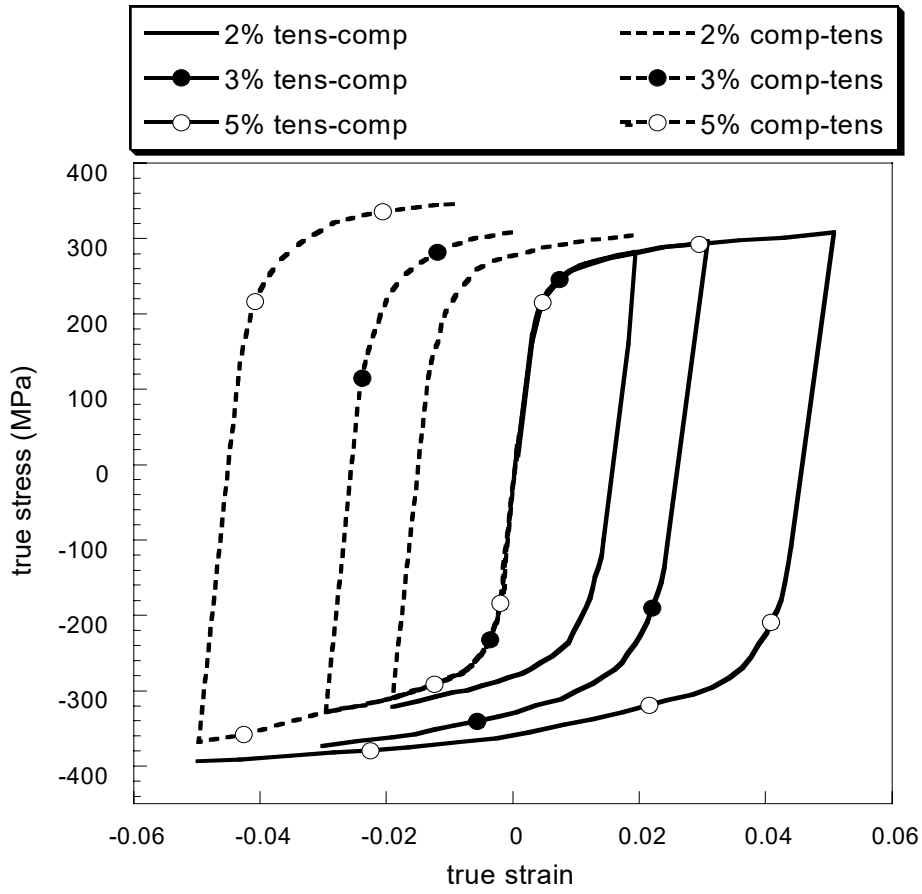

Figure 4.2. Half-cycle true-stress true-strain data for A356-T651 comparing the compression followed by tension to tension followed by compression.

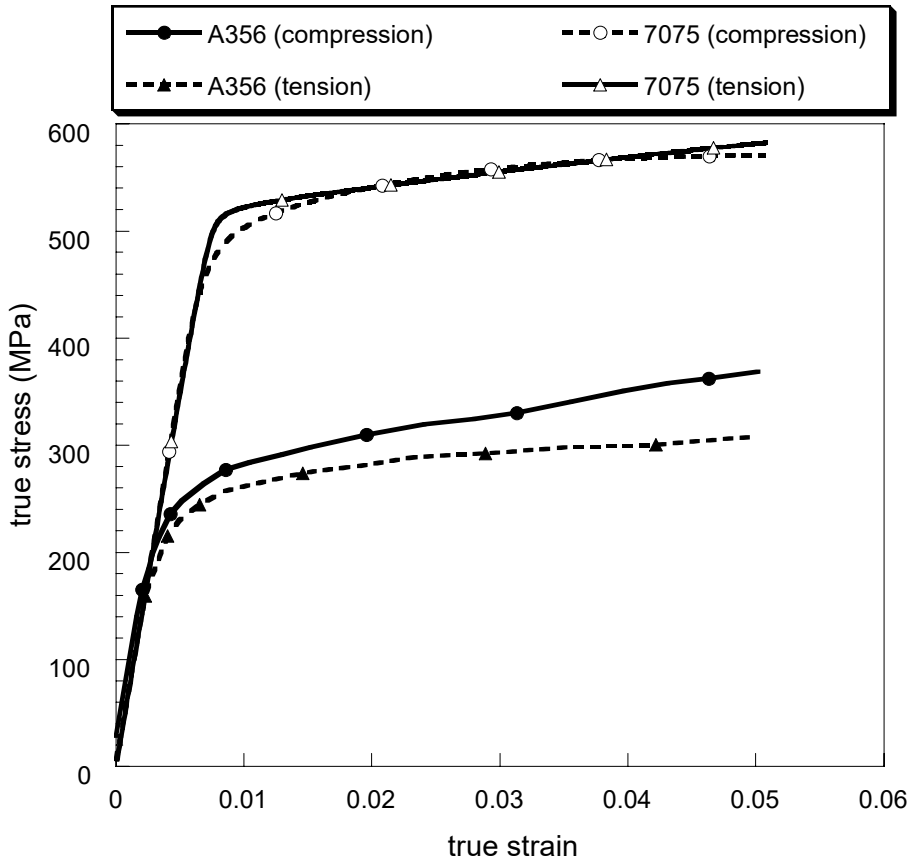

Figure 4.3. Monotonic data for A356-T651 and 7055-T651 comparing the difference between the tension and compression flow stress

Bauschinger Effect Parameter Observation

Table 2 displays the BED, BSP, BEP, and RKI that were calculated for A356-T6 and 7075-T651 from the experimental results of the tension-followed-by-compression and compression-followed-by-tension sequences for 0.2% strain offset yield definitions. For visual comparison of the Bauschinger effect, the BED is plotted versus the applied strain and shown in Fig. 4.4. When comparing the BED for both alloys, the 7075-T651 increases as the initial applied strain increases, while the A356-T6 result decreases as the initial applied strain increases. In addition, the BSP and RKI are plotted in Fig. 4.5. The

trends of the RKI parameter increase with an increasing applied strain for both alloys regardless of the loading sequence (tension-followed-by-compression versus compression-followed-by-tension). However, the BSP increases as the prestrain increases for the 7075-T651 for both loading sequences, but the BSP for the A356-T6 has different trend. As the prestrain increases, the BSP increases for the tension-followed-by-compression, but decreases for the compression-followed-by-tension. Another observation from the data shows that the A356-T6 has a higher RKI than the 7075-T651. Additional discussion of this will be addressed in chapter VI of this work. The last observation from the results in Table 2 is that the BEP is inversely related to the RKI, thus indicating that the BEP is correlated to the ratio of isotropic-to-kinematic hardening (RIK). Again the relation of BEP to RIK has not been observed in the literature.

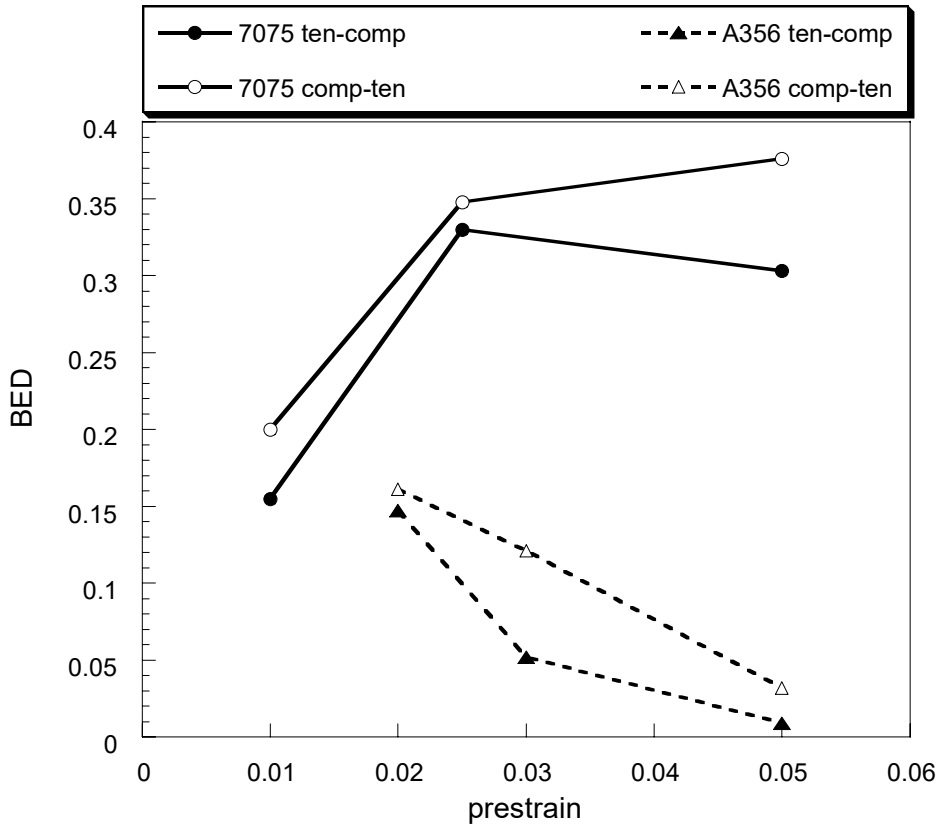

Figure 4.4. The Bauschinger Effect Definition (BED) plotted versus the maximum forward pre-strain reached before reversal.

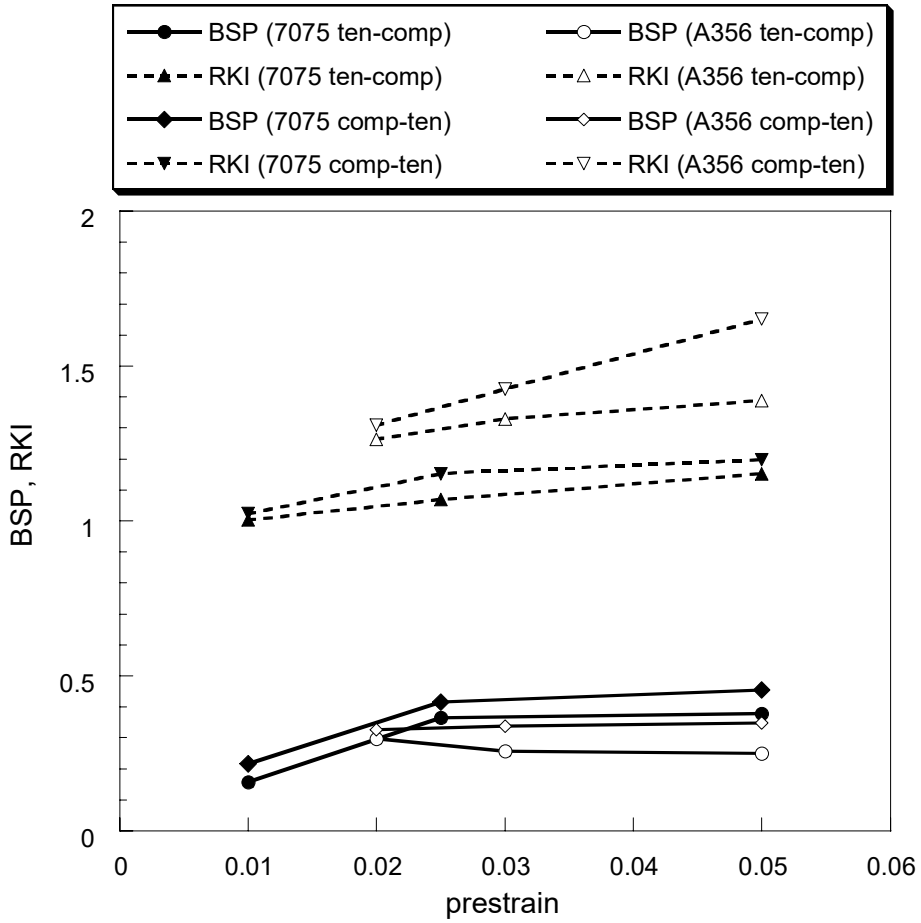

Figure 4.5. The Bauschinger Stress Parameter (BSP) and Ratio of Kinematic and Isotropic Hardening (RKI) plotted versus the maximum forward pre-strain reached before reversal for 7075-T651 and A356-T6.

To further illustrate the comparison of the data generated for this study with that in the literature, the BSP data from a cast 3xx series aluminum alloy presented by Caceres *et al*. (1996) is plotted with the A356-T6 and 7075-T651 as shown in Fig. 4.6. Clearly, the BSP values for both alloys correlate well with the Caceres *et al*. (1996) results. Although not mentioned in Caceres *et al*. (1996), it is concluded that their data is a tension-followed-by-compression sequence, because both the tension-followed-by-compression wrought and cast alloy values overlay with their data.

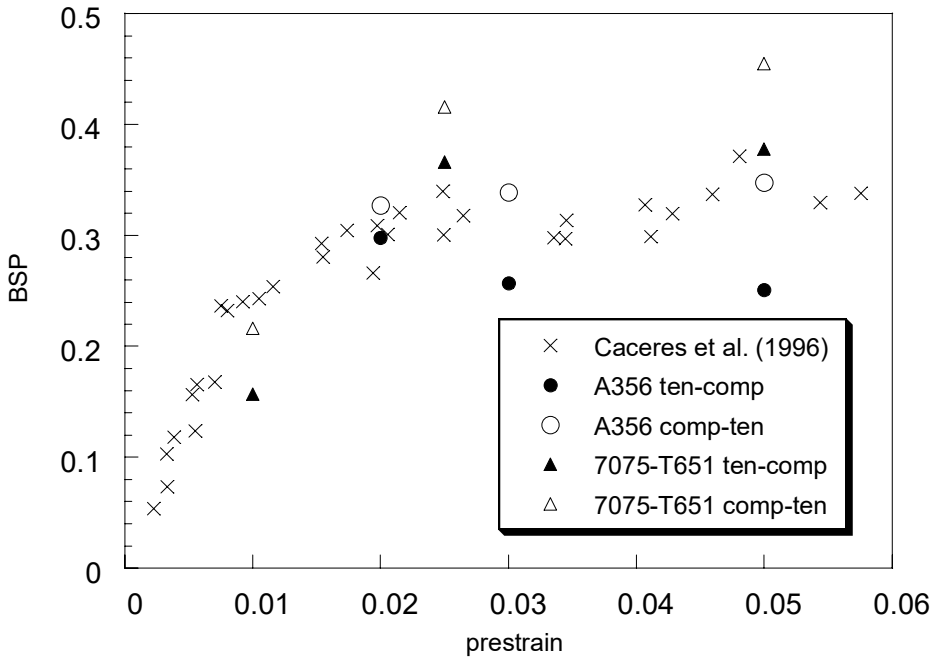

Figure 4.6. A plot of the Bauschinger Stress Parameter (BSP) as a function of the maximum forward pre-strain reached before reversal.

Table 4.1. Comparing BSP, and ratio of kinematic to isotropic hardening for the Bauschinger tests at various pre-strain levels for 7075-T651 and A356-T6 aluminum alloys.

Experiment	σ_y (MPa)	σ_r (MPa)	σ_f (MPa)	α	R	BED	BSP	BEP	RKI
Wrought Aluminum 7075-T651-T651									
1% ten-comp	520	439	521	480.2	479.0	0.155	0.157	32.987	1.003
2.5% ten-comp	520	348	549	448.5	419.7	0.330	0.366	3.481	1.069
5% ten-comp	520	363	583	472.6	410.0	0.303	0.378	1.757	1.153
1% comp-ten	498	399	508	453.3	443.2	0.200	0.216	5.404	1.023
2.5% comp-ten	498	325	556	440.6	382.2	0.348	0.416	1.983	1.153
5% comp-ten	498	311	571	440.9	368.0	0.376	0.455	1.783	1.198
Cast Aluminum A356-T6-T6									
2% ten-comp	232	198	282	240.0	190.0	0.147	0.298	0.840	1.263
3% ten-comp	232	220	296	258.0	194.0	0.052	0.257	0.594	1.330
5% ten-comp	232	230	307	268.5	193.5	0.009	0.251	0.513	1.388
2% comp-ten	248	208	309	258.5	197.5	0.161	0.327	0.828	1.309
3% comp-ten	248	218	330	274.0	192.0	0.121	0.339	0.683	1.427
5% comp-ten	248	240	368	304.0	184.0	0.032	0.348	0.533	1.652

The following definitions are present again for clarity:

$$BSP = \frac{|\sigma_f| - |\sigma_r|}{|\sigma_f|} \tag{4-1}$$

$$BEP = \tfrac{1}{2}\left\{\frac{|\sigma_f| - |\sigma_r|}{|\sigma_f| - |\sigma_y|}\right\} \tag{4-2}$$

$$BED = \frac{\sigma_y - \sigma_r}{\sigma_y} \tag{4-3}$$

$$RKI = \frac{\sigma_f + \sigma_r}{\sigma_f - \sigma_r} - 2\sigma_y \tag{4-4}$$

CHAPTER V

MATERIAL MODEL ANALYSIS

Model Correlation

The ISV plasticity-damage model constants were determined from experimental data by using a least sum-squared best-fit method. The plasticity and damage constants are shown in Appendix A. The model-experiment correlation process produced different constants for A356-T6 and 7075-T651. The constants for the hardening and kinematic and isotropic hardening equations were selected to produce the best fit of the experimental data. The comparison of the model to the experimental results for both the 7075-T651 and A356-T6 alloy are shown are shown in Fig. 5.1 and Fig. 5.2, respectively.

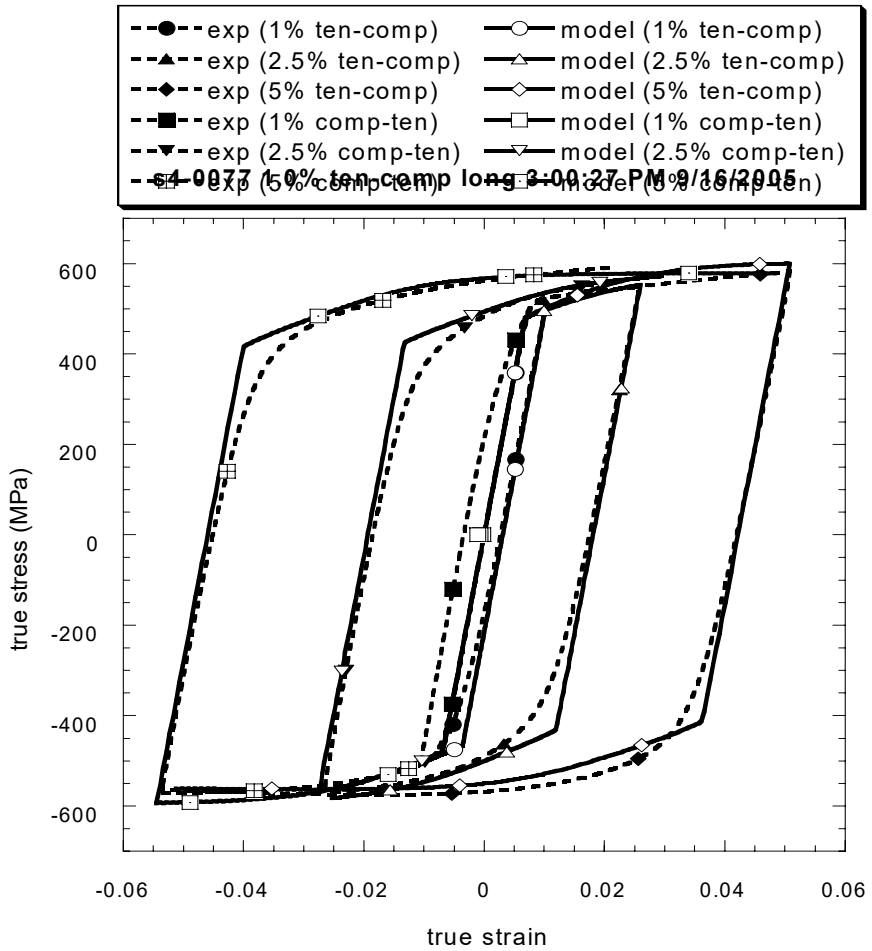

Figure 5.1. The one-element FE model using an ISV plasticity-damage model is able to capture the Bauschinger effect for 7075-T651 wrought aluminum alloy

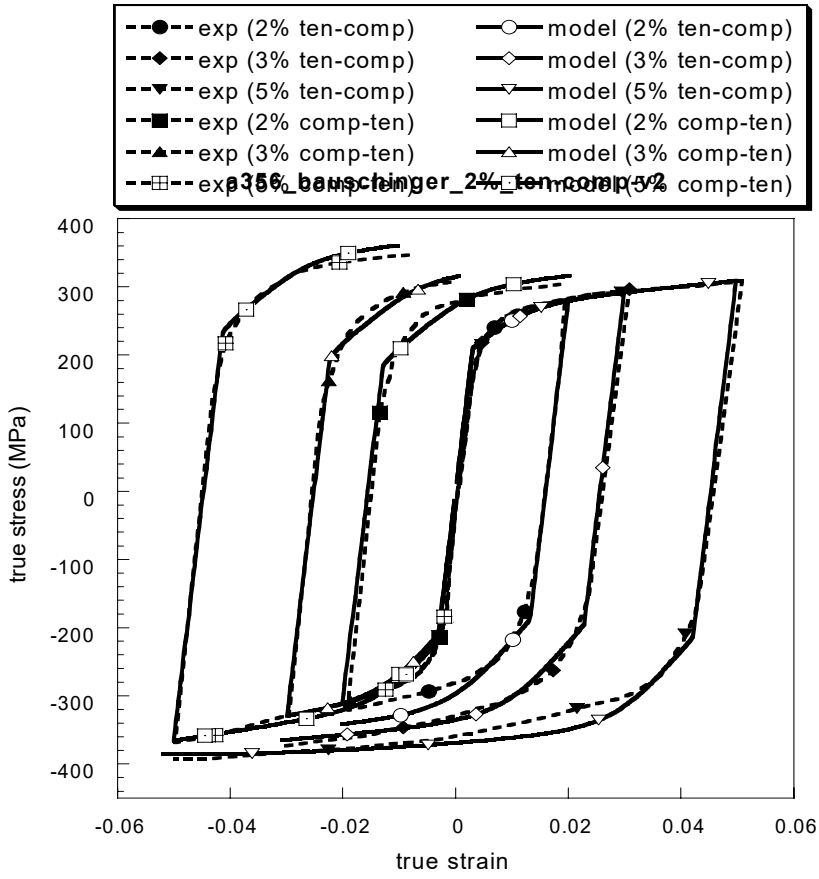

Figure 5.2. The one-element FE model using an ISV plasticity -damage model is able to capture the Bauschinger effect for A356-T6 cast aluminum alloy.

Void Nucleation Correlation

Fig. 5.3 displays the experimental results of damage progression in terms of void nucleation versus applied strain and the ISV Model nucleation rate fit of A356-T6 and 7075-T651 respectively. The damage characterization study showed that void nucleation occurred in the A356-T6 due to silicon fracture and debonding of the aluminum-silicon interface within the dendrite cells. Gall *et al.* (2000) explained that silicon fracture would occur when the defect density was high in the particles, but interface debonding would occur when the defect density was small in the particles. For the 7075-T651 aluminum

alloy, particle fracture and interface debonding of the iron-rich second phase were observed to be the main sources of void nucleation.

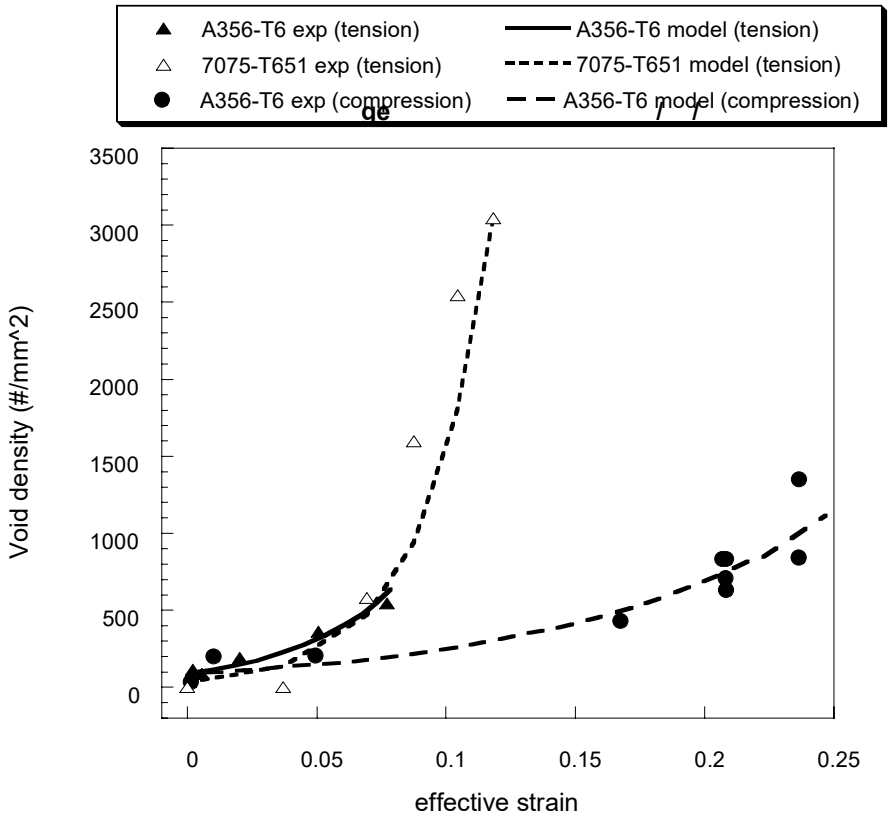

Figure 5.3. A comparison of the damage nucleation model and experimental data of the void/crack density versus strain for A356-T6 and 7075-T651. The plot shows greater void/crack nucleation for tension than compression for cast A356 aluminum alloy

The difference observed on the tension versus compression prestrain was due to the intimate relation of the damage nucleation difference coupled with the hardening rate difference. The local dislocation density that built up at particles relaxed as particles cracked or debonded in turn affecting the work hardening rate. For the A356 aluminum alloy, the damage nucleation rate was higher and the work hardening rate was lower when comparing tension to compression. Also, the damage nucleation rate was very

similar for A356-T6 and 7075-T651 under tension even though the average particle size was different, the aspect ratio of the particles was different, and the volume fraction was different. Unfortunately, at the time of publication the compression nucleation rate data for the 7075-T651 was unavailable. However, for this study, the compression damage nucleation rate for the 7075-T651 was assumed to be the same as the A356-T6.

CHAPTER VI

DISCUSSION

Clearly several trends can be discerned when studying the Bauschinger effect on these aluminum alloys. The RKI, BSP, and BEP for 7075-T651 aluminum and RKI and BSP for A356 aluminum were greater for compression-followed-by-tension than tension-followed-by-compression experiments. As the prestrain increased, the reverse yield stress increased for the A356-T6 aluminum alloy but decreased for the 7075-T651 aluminum alloy. In addition, as the prestrain increased, whether tension or compression, the RKI increased, but the BEP decreased. Since the BEP has an inverse relation with RKI, it can be thought to correlate to the ratio of isotropic hardening to kinematic hardening (RIK). Also, since RKI increases with increasing prestrain, the growth of the kinematic hardening is greater than the isotropic hardening, meaning that anisotropic hardening is growing more than isotropic hardening for these two alloys. This finding is a bit surprising because aluminum alloys are FCC structures and have high stacking fault energies leading to enhanced cross-slip activity. If the BEP is the most appropriate definition from Bauschinger's original work, the BSP and RKI represent 7075-T651 more accurately but the BEP represents A356-T6 more accurately. As such, different definitions represent different materials much better than others.

The tension prestrain incurred a larger damage nucleation rate and a lesser work hardening rate than the compression prestrain as shown in Fig. 5.3. This tension-compression asymmetry demarks that these aluminum alloys are history dependent and that material models should include history dependence if path dependence is experienced. Although the nonlinear, anistropic plasticity coupled with damage evolution give different complex responses in nonmonotonic loading sequences, the internal state variable plasticity model given by Bammann (1990, 1993, 1996) and updated with damage by Horstemeyer *et al*. (2001) represent the mechanical behavior fairly well. The experimental data illustrated in Figures 5.1 and 5.2 can be used to assess plasticity-damage models.

The A356-T6 aluminum alloy, with a larger number of particles exhibited a larger RKI compared the 7075-T651, which has a more prominent grain boundary microstructure with fewer particles. However, as the forward applied strain increases for both alloys, the rate of increase of the RKI diminishes slightly**.** This reduction in the rate of the RKI can be attributed to the accumulation of damaged particles, where the cracked/debonded particles reduce the work hardening rate. Hence, there seems to be a relationship between the rate at which damage is occurring and plasticity in terms of kinematic and isotropic hardening.

The RKI calculated from the experimental flow stress for both alloys was compared to the RKI taken from the ISV finite element simulations and is shown in Fig. 6.1. The plasticity-damage model RKI was determined by integrating the flow stress over the entire strain path. The experimental data and the model RKI agree very well for

the 7075-T651. Not only do the numerical values for the model correlate well with the experimental RKI, but there is also a similar increasing trend as the forward prestrain increases. In contrast, the experimental and model RKI values for the A356-T6 alloy have opposite trends as a function of prestrain. One possible explanation for this discrepancy is that the flow stress for the A356-T6 has more of a contribution from the damaged particles than the 7075-T651 alloy.

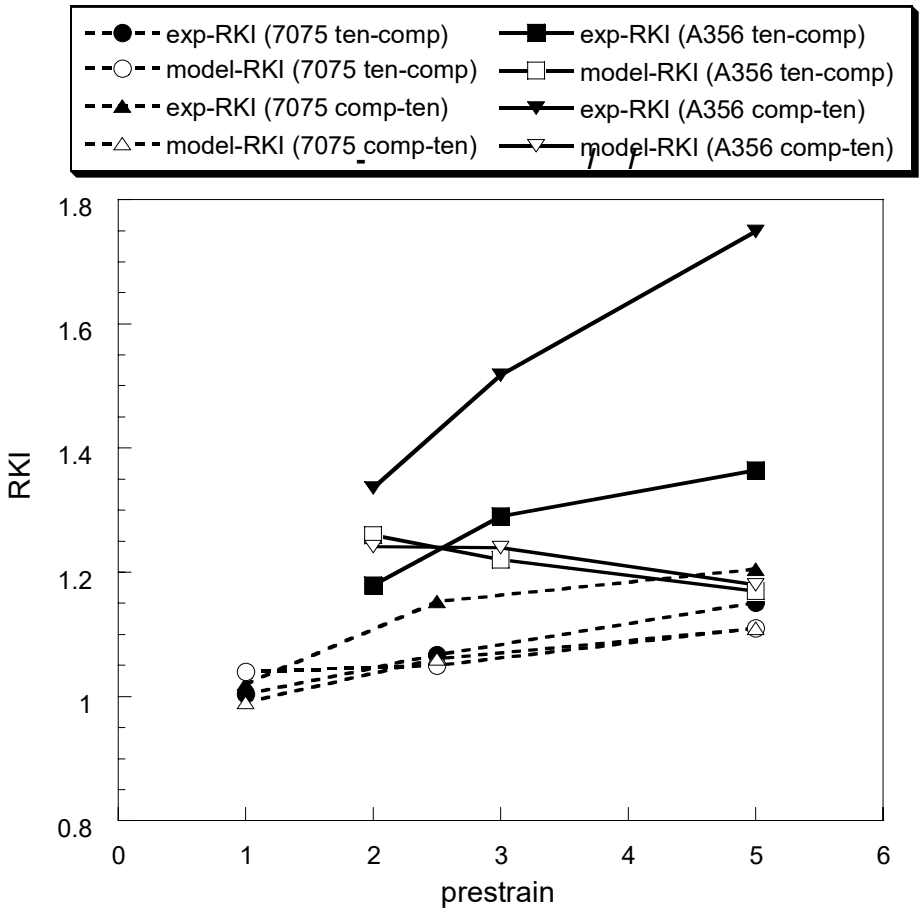

Figure 6.1. The experimental and finite element model of the Ratio of Kinematic and Isotropic Hardening (RKI) plotted versus the maximum forward prestrain reached before reversal for 7075-T651 and A356-T6.

It is believed that the 7075-T651 would have greater anisotropy (higher RKI or BSP) if the alloy had as many second phase particles as the A356-T6. Likewise, without the large percentage of silicon particles, the A356-T6 would be much more isotropic (lower RKI and BSP) in nature. However, some level of anisotropic behavior is excepted as displayed by pure aluminum. For alloys like 7075-T651 and A356-T6 that have particles and granular microstructure, the anisotropic behavior would likely exist even without the presence of the second phase particles and inclusions. For instance, Stout and Rollet (1990) showed that pure single phase aluminum would display a slight decrease of reverse yield, thus experiencing a weak, but still apparent, Bauschinger effect. Therefore, it is concluded that the main contributor of Bauschinger effect in these two alloys is a function of the precipitate phases that impede dislocation motion coupled with the damaged constituent particles that reduce the work hardening rate.

CHAPTER VII

SUMMARY AND CONCLUSIONS

The purpose of this work was to capture the Bauschinger effect by using an internal state variable constitutive model that includes the effect of isotropic and kinematic hardening and damage state accumulation. Other researchers have modeled the Bauschinger effect using only hardening laws. However, experimental evidence has been presented that shows that the stress state is also dependent on damage nucleation resulting from constituent particles fracturing or debonding from the aluminum matrix.

Experiments in tension-followed-by-compression and compression-followed-by-tension were performed on rolled and cast aluminum alloys. Several new definitions as well as existing parameters were employed to quantify the degree of the Bauschinger effect. To better understand the contribution of the kinematic and isotropic hardening to the plastic flow stress, the ratio of the kinematic-to-isotropic hardening parameter was employed. Based on the experimental work, both alloys (7075-T651 and A356-T651) displayed higher RKI, BSP, and BEP in compression-followed-by-tension compared to tension-followed-by-compression. In addition, the experimental results showed that as the forward strain increased, the Bauschinger effect increased for the 7075-T651, and decreased for the A356-T6. Experimental damage nucleation results showed a path

dependence that affects the stress/strain asymmetry and suggested a link between the RKI and damage nucleation rate.

No longer can the Bauschinger effect be modeled without the inclusion of a void/crack nucleation model that can distinguish between tension and compression and apply to different material microstructures. An internal state variable plasticity-damage model was introduced, along with pertinent equations and assumptions, and was able to reproduce the evolving Bauschinger effect as the damage rate evolves.

REFERENCES

Abel A, Muir H. Phil Mag 1972;ser 8: 489-504.

Abel A. Material Forum 1987;10 No.1: 11-26.

Aran A, Demirkol M, Karabulut A. Mater Sci Eng 1987;89:L35.

Arsenault RJ, Wu SB. Mater Sci Eng 1987;96:77-88.

Atkinson JD, Brown LM, Stobbs WM. Philos Mag 1974;30:1247.

Bammann DJ, Aifantis EC. Nuclear Engineering and Design 1989;116: 355-362.

Bammann, DJ Appl Mech Rev No. 5, Part 2, Eds. Krempl E and McDowell DL, 1990; 43: S312-S319.

Bammann DJ, Chiesa ML, Horstemeyer MF, Weingarten LI. eds. N. Jones and T. Weirzbicki, Structural Crashworthiness and Failure, Elsevier Applied Science, 1993.

Bammann DJ, Chiesa ML, Johnson GC. App Mech eds, Tatsumi, Wannabe, Kambe. Elsevier Science 1996: 256-276.

Bate PS, Wilson DV. Acta Metall 1986;34:1097.

Bauschinger J. Civilingenieur 1881, 27:289.

Brown LM, Stobbs WM. Philos Mag 1971;23:1185.

Brown LM, Stobbs WM. Philos Mag 1971;23:1201.

Brown LM. Scripta Metall 1977;11:127.

Caceres CH, Griffiths JR, Reiner P. Acta Metall 1996;44: 15-23.

Choteau M, Quaegebeur P, Degallaix S. Mech Mater 2005;37: 1143-1152.

Corbin SF, Wilkinson DS, Embury JD. Mat Sci and Eng 1996:A207: 1-11.

Dighe MD, Gokhale AM, Horstemeyer MF. Metall. Mat. Trans A 2002;33A: 555-565.

Embury JD. Metall Trans A 1985;16A: 2191-2200.

Embury JD. Mater. Forum 1987; 10: 27-33.

Gall KA, Horstemeyer MF, Van Schilfgaarde M, Baskes. MI J Mech Phys Solids 2000; 48: 2183-2212.

Gall KA, Yang N, Horstemeyer MF, McDowell DL, Fan J. Metall Trans A 1999:30A; 3079-3088.

Hasegawa T, Yakou T, Kocks UF. Mater Sci Eng 1986;81:189.

Horstemeyer MF. Scripta Mat 1998;39:1491-1495.

Horstemeyer MF. J Comp Aid Matl Des 2003 ; 36 :13-34.

Horstemeyer MF From Atoms to Autos: Part I: Monotonic Loading Conditions, Sandia National Lab 2001: 6.6-11.

Horstemeyer MF, Gohkale AM. Int. J. Solids and Struct 1999; 36: 6-11.

Horstemeyer MF, Lathrop J, Gokhale AM, Dighe M. Theor and Appl Fract Mech 2000; 33: 31-47.

Horstemeyer MF, Ramaswamy S, Negrete M. Mech Mater 2003;35: 675-687.

Horstemeyer MF, Wang P. J Comp Aid. Mat Des 2003;36:13-34.

Lloyd DJ. Acta Metall 1977;25: 459-466.

Margolin H, Hazaveh F, Yaguchi H. Scripta Metall 1978;12:1141.

Masing G. Wiss Vero. Siemens-Konzern 1923;3:231.

Miller, MP, Harley EJ, Bammann DJ. Int. J. Plas 1999;15: 93-117.

Moan GD, Embury JD. Acta Metall 1979;22: 903-914.

Mollica F, Rajagopal KR, Srinivasa AR. Int. J. Plas 2001;17: 1119-1146.

Ono N, Tsuchikawa T, Nishimura S. Mater Sci Eng 1983;59:223

Pedersen OB, Brown LM, Stobbs WM. Acta Metall 1981;29: 1843-1850.

Rao MK, Murty GS. Trans of the Indian Institute of Metals 1982;35: 543-547.

Reynolds AP, Lyons JS, Metall. Mat. Trans A 1996;28A: 1205-1211.

Shiratori, E, Ikegami K, Yoshida, F, J. Mech. Phy. Solids 1979;27:213-229.

Sleeswyk AW, Kemerink GJ. Scripta Metall 1985;19: 471-476.

Sowerby R, Uko DK. Mat. Sci. Eng. 1979;41: 43-58.

Sowerby R, Uko DK, Tomita Y. Mater Sci Eng 1979;41:43.

Stoltz RE, Pelloux RM. Metall Trans A 1976;7:1295.

Stout AG, Rollett AD Metall. Trans A 1990;21A: 3201-3213.

Thakur A, Nemat-Nasser S, Vecchio KS. Acta Mater 1996;44: 2797-2807.

Vincze G, Rauch EF, Gracio JJ, Barlat F, Lopes AB. Acta Mat 2004;53: 1005-1013.

Woolley RL. Phil Mag 1953;44: 597-618.

Xiang Y, Vlassak JJ. Scripta Mat 2005;53:177-182.

Appendix A

A356-T6 and 7075-T651 Model Constants

Table A.1. Microstructure-property (elastic-plastic) model constants for A356-T6 and Aluminum 7075-T651.

	Constants	A356-T6	7075-T651
Constants for J/B formulas for G and K	G	25920	27010
	a	1	1
	Bulk	67630	70290
	b	0	58600
	melt temp	5556	1494
Specifies the yield stress	C1	0	0
	C2	0	0
	C3	210	480
	C4	0	0
	C5	0.00001	1
	C6	0	0
Kinematic hardening and recovery terms	C7	1.5	0.6
	C8	0	0
	C9	7976	4000
	C10	0	0
	C11	0	0
	C12	0	0
Isotropic hardening and recovery terms	C13	0.0075	13.00
	C14	0	0
	C15	1100	6000
	C16	0	0
	C17	0	0
	C18	0	0
Hardening & recovery cons.	Ca	0	0
	Cb	-0.5	-.1
Temperature	init.temp	297	297
	heat gen. Coeff.	0	0

Table A.2. Microstructure-property (damage) model constants for A356-T6 and 7075-T651 aluminum alloys.

	Constants	A356-T6	7075-T651
McClintock Void Growth	void growth exp	0.3	0.003
	init. Rad.	0.0002	0.000001
Nucleation	tors const. a	615369	0
	nuc const b	58630	46000
	nuc const c	30011	12000
	nuc coeff	90.6	33.2
	fract. Toughness	17.3	27
	part. Size	0.000004	0.0002
	part. Vol fract.	0.07	0.02
Coalescence	cd1	1	1
	cd2	0	0.023
	dcs0	20	40
	dcs	20	40
	dcs exp. Zz	0.0509	0.00509
CA pore growth	init. Void vol. Fract.	0.0001	0.0001
Nucleation	nuc. Temp. depend.	0.0035	0.0035
Coalescence	coal. Temp. depend	0.009	0.009
Yield strength Adjustment terms	c19	-5	0
	c20	-0.38949	0